

A 3-DOF Neuro-Adaptive Pose Correction System For Frameless and Maskless Cancer Radiotherapy

Lekan Ogunmolu¹, Adwait Kulkarni², Yonas Tadesse², Xuejun Gu³, Steve Jiang³, and Nicholas Gans¹

Abstract—Precise patient positioning during treatment of cancers of the head and neck region is fundamental to a successful clinical removal of malignant tumors. We propose a 3-DOF soft-robot position correcting system to correct head deviations along 3 axes. The robot consists of inflatable air bladders to move the head while ensuring patient safety and comfort. The robot is controlled with an based off an adaptive-neuro controller consisting of a state feedback regulator, a command reference tracking component, and a function approximator that compensated for parametric and non-parametric system errors in real-time. Feedback is provided by a precise 3D stereo camera for surface imaging of the head. We implement the controller on a 3D printed head-and-neck simulator and demonstrate that our control exhibits real-time learning to correct positioning deviations.

I. INTRODUCTION

Cancers of the head and neck (H&N) are very deadly, resulting in over 10,000 deaths annually in the US alone. Radiation-based treatment of the H&N region often involves intensity-modulated radiotherapy (IMRT). By modulating radiation dosage and shaping treatment beam to the precise size of tumor cells, IMRT carefully targets organs, while minimizing toxicity and exposure of organs at risk. IMRT is increasingly being used alongside image guided radiotherapy (IGRT) to assure precision of dosage targets. To ensure precise and accurate dosage administration, a patient is positioned on a treatment table after dosage planning by a physician, and a rigid robotic couch is used for motion alignment during surgery. While conventional RT uses rigid immobilization techniques such as masks, frames, arm positioning devices or vacuum mattresses [1], IGRT methods employ ultrasound, 3D imaging systems, 2D X-ray devices and/or computed tomography to instantly amend positioning errors, and to improve daily radiotherapy fractions' precision.

Precise, accurate and repeatable patient positioning is therefore crucial in RT treatments when escalation of dose is necessary in a target volume and exposure of adjacent organs is to be minimized. Because it does not require rigid masks and body fixators, IGRT is more comfortable for the patient

as well as more accurate with the aid of highly accurate localization systems. Sterzing [2], after an extensive review of IGRT methods, found IGRT to be more precise and safer than conventional radiotherapy. But setup errors (interfractional) or patient motion (intrafractional) errors often need to be accounted for during RT. While intrafractional errors can be minimized by highlighting the importance of voluntary stillness to the patient, suitable means of immobilization and positioning correction are necessary when the patient moves involuntarily or sleeps; this assures precise and accurate targeting of critical organs while keeping the patient comfortable during treatment. Frameless and Maskless (F&M) IGRT is promising because it minimizes invasiveness and reduces setup times while comfortably positioning the patient.

Following our recent investigative studies, [3], [4], on 1-DoF motion compensation soft-robot systems, we present a 3-DoF soft robot system to address involuntary intrafractional 3-DoF correctional motions of the head and neck (H&N) region during F&M RT. Soft robot systems are elastomeric active and reactive nonlinear compliant systems that are suitable to the task of human-machine interaction in H&N cancer RT as they can dynamically change their stiffness and activate their surfaces to provide a desired motion on a human body part. Their characteristic morphological computation properties [5] make them suitable for autonomous control including inflation, deflation and reaching. Exhibiting highly nonlinear dynamics, controlling them for precise actuation can be challenging. Deriving a model-driven, metric-based approach may work in low-level, highly structured environments; however, system parameters change with different patients' head and upper torso anatomy such that achieving dynamical precise control becomes a problem for a model-driven approach. The introduction of learning-based modeling techniques in pattern recognition and regression tasks hold the promise of going beyond current expert-driven methods in adaptive control theory. Reliable high-parameter space adaptive-control methods rely on open-loop adaptation so that real-time learning is discarded. Such adaptive control methods require extensive design techniques as shown by the CH-47 helicopter which had ninety controllers for ninety different flight envelopes [6], with a linear interpolation between the controllers used in modifying the behavior of the helicopter in flight. For higher-level tasks, it suffices to learn the underlying system dynamics through *imitation learning*, *i.e.* data-driven approaches, than building hand-engineered, finite-state machines to implement intended behaviors.

This work presents therefore presents an adaptive neuro-controller that learns the system model in real-time and

*This work was supported by the Radiation Oncology Department, UT Southwestern, Dallas, Texas, USA

¹Lekan Ogunmolu and Nicholas Gans are with the Department of Electrical Engineering, University of Texas at Dallas, Richardson, TX 75080, USA {olalekan.ogunmolu, ngans}@utdallas.edu

²Adwait Kulkarni and Yonas Tadesse are with the Department of Mechanical Engineering, University of Texas at Dallas, Richardson, TX 75080, USA {axf151530, ytt110030}@utdallas.edu

³Xuejun Gu and Steve Jiang are with the Department of Radiation Oncology, University of Texas Southwestern Medical Center, Dallas TX 75390, USA {Xuejun.Gu, Steve.Jiang}@utsouthwestern.edu

generates an adaptive control law to provide bounded tracking of set trajectory. The controller corrects intrafractional motions along three defined axes namely head pitch, roll, and elevation angles while a patient lies in a supine position above a table. We use three inflatable air bladders (IABs), actuated through a system of inlet and outlet solenoid proportional valves. The controller uses state feedback to provide bounded stability of states, a reference trajectory component provided command tracking and a neural-network component adaptively converged states that start outside of the sphere of stability into the region of stability. A stereo-camera is used to measure head pose and we conduct experiments to validate the proposed bio-pneumatic system and controller.

This paper is organized as follows: section II presents related work, section III describes the hardware setup, IV describes the vision segmentation algorithm and 3-DOF pose estimation, while section V describes the adaptive-neuro control algorithm formulation. We discuss experiments in VI and provide discussions and conclusions in VII.

II. RELATED WORK

There has been related research aimed at studying the feasibility of non-rigid immobilization devices during cranial stereotactic radiosurgery (SRS). These fall largely under *inspection-based* non-rigid immobilization devices accompanied by real-time patient motion monitoring systems, and *correction-based* non-rigid immobilization systems.

Inspection-based Systems: In [7], Cervino et al. used expandable foams that fit a patient’s head while leaving the face open. Patient set-up was performed using computed tomographic (CT) scan fitted with CBCT before treatment. They found an average treatment time of 26 minutes with patients who slept during experiments taking longer as a result of involuntary movements. In [8], the authors evaluated the accuracy of a head mold that minimally immobilized a patient’s H&N region while leaving the face free in a controlled positioning experiment with volunteers. 3D surface reconstruction imaging system was used in monitoring patients’ position so that treatment was stopped whenever motion exceeded a defined threshold. While the monitoring system showed great clinical accuracy, it required high patient cooperation to achieve immobilization. Li et al. in [9] compared using a head mold + open face-mask and a head mold + mouthpiece to ascertain the reduction in setup time, and to quantify residual rotations and positioning errors whilst correcting the patient head motion during treatment via monitoring. They reported the head mold and open face mask system could restrict head motions to within $0.6^\circ \pm 0.3^\circ$ with the time spent on in-situ motion corrections limited to 2.7 ± 1.0 min. Again, this involved no closed-loop control.

Correction-based Systems: In [10], a 4-DOF motion correction system was used in the real-time motion compensation of a phantom and in human trials. An optical sensing system tracked the pose of the head and a decoupling control law regulated the xyz -translational and pitch motions of the head. They reported target accuracy of 0.5mm and 0.2° with the decoupling controller for each axis of the 4-DOF motion.

This system relies on stepper motor actuators and other electro-mechanical (EM) components positioned under the patient’s H&N region. These devices have the undesirable effect of attenuating treatment beams during RT, and as a result are not recommended during clinical procedure. The presence of the EM stages can significantly reduce the efficacy of the incident radiation targeted to tumor cells.

To address these concerns, we proposed soft-robot actuators for H&N motion compensation during F&M cancer radio-therapy [3], [4] actuated by pneumatic valves which are kept away from the head. Plastic hoses and silicone connectors convey air into and out of the soft robots that laid beneath the head so that our motion correction system does not interfere with planned dosage from the treatment beam. In our evaluations set-up, we used pneumatic valves mounted on a movable plywood and connect these to the soft robots with long silicone tubes so that the medical physicist can separate EM components from the patient as deemed necessary during treatment. While our previous works related to controlling the 1-DoF motion of the head along the z -axis, here we address the 3-DOF control of the head using a surface reconstructing sensor and control the pose of the head to follow set trajectories in real-time.

III. HARDWARE DESIGN OVERVIEW

The actuation mechanism consists of three custom-designed inflatable air bladders (IABs) made from elastomeric polymers. One IAB (beneath the top of the head) is 180mmx280mm when flat and can safely inflate to a width of at around 75mm. The other two IABs are 180mmx140mm. The IABs consist of inflatable rubber covered by a breathable foam pad for comfort. These were medical IABs commercially obtained and modified for size and to have separate inlet and outlets. The inlets and outlets were connected with crack-resistant polyethylene tubing (1/8” ID and 1/4” OD), which can sustain a pressure up to 320psi.

Each hose leads to a proportional solenoid valve, which is in turn connected to rectangular manifolds (one manifold to the inlet supply and the second to the outlet supply). We used four Dakota electromagnetic valves (Model PSV0105, Dakota Instruments, Orangeburg, NY, USA) and two current-controlled proportional solenoid valves (Model PVQ33-5G-23-01N, SMC Co., Tokyo, Japan). A regulated air canister supplies constant air pressure at 15psi to the inlet-air conveying manifold, while a suction pump supplies vacuum pressure at 12 psi to the valves that removed air from the bladders. The air rate of flow into or out of each bladder was controlled from PWM signals (for the Dakota valves) and current source signals (for the PVQ valves) generated from a National Instruments (NI) myRIO microcontroller. Current amplifying and voltage regulator circuits were custom-designed in our lab.

A head was 3D printed, measuring 155mm in breath, 240mm in length and 200 mm in depth. This size is between 50% and 75% for adult males and 99% of adult females. It was weighted to 5kg, which is above average, but reasonable head mass. Since the head is 3D printed, we can experiment

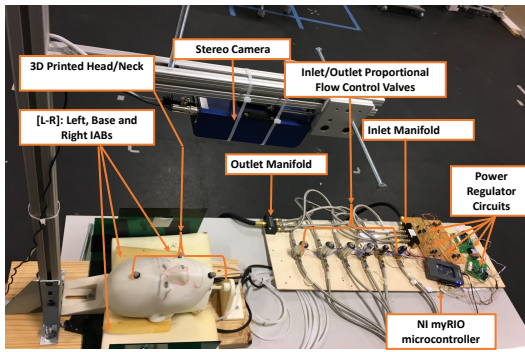


Fig. 1: Hardware Description

various head sizes in future work. The head is fitted with a ball-joint in the neck to replicate motion of the human head about the neck.

An Ensenso 3D camera is mounted above the head to measure the pose of the head in real time. All vision processing, systems modeling and control laws were computed on a CORSAIR PC. We publish the control law, given a reference trajectory, using the ROS middleware installed on the RIO and PC. The RIO subscribes to control laws on a ROS topic and sends position commands to the head based on given reference. The soft robot system is shown in Fig. 1.

The reference frame of the head is described as follows: the pitch/y-axes points from the left ear out of the right ear, the yaw/z-axes points from the forehead through the back of the head, and the roll/x-axes goes from the neck through the top of the head. The left and right bladders control the yaw and x-axes motions while the bladder underneath the head, henceforth referred to as the base bladder, controls the pitch- and z-axis motions.

IV. VISION-BASED POSE ESTIMATION

The mannequin head lies in a supine position above a planar table as shown in Fig. 1. We employ a 3D camera from Ensenso GmbH (model N35) to reconstruct the surface image and measure head pose. The N35 camera captures multiple image pairs during exposure; each image pair is made up of different patterns, controlled by piezo-actuators. A stereo-matching algorithm gathers the information from all image pairs after capture to produce a high-resolution point cloud (PCL) of the scene [11]. We mount the 3D sensor directly above the head during our experiments for face tracking.

A. Face Segmentation

The dense point cloud of the scene has (i) marked jump in rendered points along the z-axis of the camera; this is because of the single view angle by the camera; (ii) the scene clutter and lack of multiple camera view angles does not affect the representation of the face; (iii) thus, through spatial decomposition of the scene, we can separate the face from the scene. However, the point cloud is computed from monochromatic IR image pairs (with no texture information) making morphological operations difficult; due to the

multiple image pairs used in 3D reconstruction to generate a highly accurate measurement, the camera is limited to a maximum frame rate of 10Hz. Inspired by Rusu’s work [12], we divide the segmentation problem into stages, with each stage involving segmenting out candidates that do not belong to the object we want to identify (the frontal face) in the scene. Our engineering philosophy in the segmentation phase is inspired by spatial decomposition methods that determine subdivisions and boundaries to allow retrieval of data that we want given a measure of proximity. In this case, we know that the location of the table cannot exceed a given height during experiments and the camera’s position is fixed while the head moves based on bladders’ actuation. Separating objects that represent planar 2D geometric shapes from the scene therefore simplifies the face segmentation algorithm. By finding and removing objects that fit primitive geometric shapes from the scene, clustering of the remaining objects would yield the face of the patient in the scene. We fit a simplified 2D planar object to the scene such that searching for points $\mathbf{p}_i \in \mathcal{P}$ that support a 2D plane can be found within a tolerance defined by the inequality $0 \leq |d| \leq |d_{max}|$, where $|d_{max}|$ represents a user-defined threshold to segment out [12].

We proceed as follows:

- The point cloud of the scene was acquired from the computed disparity map of the two raw camera images;
- To minimize sensor noise whilst preserving 3D representation, the acquired point cloud was downsampled using a SAmple Consensus (SAC)-based robust moving least squares algorithm (RMLS) [12, §6];
- We then searched for the edges of 2D planar regions in the scene with Maximum Likelihood SAmple Consensus (MLE-SAC) [13], and we bound the resulting plane indices by computing their 2D convex hull;
- A model fitting stage extrudes the computed hull (of objects lying above the 2D planar region) into a prism model based on a defined L_1 Manhattan distance; this gives the points whose height threshold is about the region of the face in the scene [14];
- We then cluster the remaining points based on a heuristically determined L_2 distance between points remaining within the polygonal plane. The largest cluster gives us the face.

The result of the resampling algorithm is shown in the top-right image of Fig. 2.

To simplify the complexity of the planar structure in the scene, the table is modeled as a 2D planar geometric primitive so that finding points that fit a defined model hypothesis involves estimating a single distance to the frontal plane of the table surface rather than multiple points if the model was represented with points. Searching for horizontal planes that are perpendicular to the z-axis of the head is carried out using the maximum likelihood SAC [13] algorithm implemented in the PCL Library [15] to generate model hypotheses. The plane segmentation algorithm is defined in Table I. The plane segmentation process is run once. Once the plane

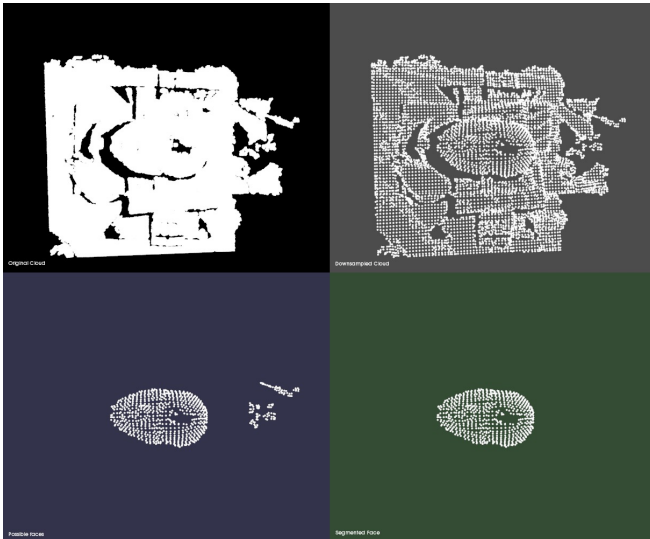


Fig. 2: [Top-left]: Dense point cloud of the experimental setup scene. [Top right]: Downsampled cluttered cloud of the left scene. [Bottom-left]: Using RANSAC, we searched for 2D plane candidates in the scene and compute the convex hull of found planar regions. We then extrude point indices within the hull into a prismatic polygonal model to give the face region. [Bottom-right]: An additional step clusters the resultant cloud based on a Euclidean distance. The largest cluster is taken to be the face.

TABLE I: Plane Segmentation Algorithm

1. **for** $i = 1$ to N **do**
2. sample non-collinear points $\{p_i, p_j, p_k\}$ from \mathcal{P}
3. calculate the model coefficients $ax + by + cz = d$
4. find distances from all $\mathbf{p} \in \mathcal{P}$ to the plane (a, b, c, d)
5. store points $\mathbf{p}^* \in \mathcal{P}$ that satisfy the model hypothesis, $0 \leq |d| \leq |d_{max}$.
6. **return** maximum of the stored points \mathbf{p}^* .

model is found, its indices and those of objects lying above it are separated and stored in separate data structures. Every subsequent iteration consists of (i) computing the 2D convex hull of point indices of objects above the table using the *Qhull* library¹, (ii) using a pre-defined prismatic model candidate to hold extruded points to the approximate facial height above the table; and (iii) separating the face from every other point in the resulting cloud through the Euclidean clustering (EC) method of [16]. A distinct point cluster is defined if the points in cluster $C_i = \{\mathbf{p}_i \in \mathcal{P}\}$ and cluster $C_j = \{\mathbf{p}_j \in \mathcal{P}\}$ satisfy the L_2 -distance threshold

$$x \leq \min \|\mathbf{p}_i - \mathbf{p}_j\|_2$$

Finding the face in the scene after carrying out EC algorithm is a question of finding the largest index in the list \mathcal{C} . This takes $O(n)$ time for n clusters. The face segmentation results are presented in Fig. 2. We then compute the Cartesian position of the face with respect to the camera origin by taking the center of mass of the segmented facial region (bottom-right image of Fig. 2). This is obtained by calculating the

¹The Qhull library: <http://www.qhull.org/>

mean-value of all the points in the resulting cloud (≈ 600 points on average).

B. Head Pose Estimation

With the facial point cloud segmented, we determine the pose of the head. All point coordinates are with respect to a Cartesian frame in the stereo camera. We consider the world frame to have an origin at the centroid of the head when all IABs are at ambient pressure, with the axes oriented as described in Section III. The current head frame has its origin at the centroid of the head under current measurements, with the axes again as described in Section III, and found through the distribution of segmented points. The pose of the face is described by tuples $\{x, y, z, \theta, \phi, \psi\}$ with respect to the world frame. Given the 3-DOF setup, we choose to control three states of the head, namely z and θ (pitch) and ψ (roll).

V. CONTROL DESIGN

Our control philosophy is governed by the feedback regulation problem coupled with an estimation of the head pose given a priori information about the system's states and past control actions. We propose an adaptive control problem in a Bayesian setting, which given an initial prior distribution, minimizes a cost criterion as the expected value of the head position given the system's states and past controls. We consider the pwm voltages and current source signals that powered the valves as input, \mathbf{u} , and the head pose as the output, \mathbf{y} and a model disturbance $\mathbf{w}(k)$. Our goal is to build a function approximator model $\hat{f}(\mathbf{u}(k-d), \mathbf{y}(k), \mathbf{w}(k))$ from lagged input and output experimental data that satisfy

$$A(z)\mathbf{y}(k) = B(z)\mathbf{u}(k-d) + C(z)\mathbf{w}(k) \quad k, d \geq 1 \quad (1)$$

where

$$\begin{aligned} A(z) &= 1 + a_1 z + \dots + a_n z^n, \\ B(z) &= b_0 + b_1 z + \dots + b_m z^m, \quad b_0 \neq 0 \\ \text{and } C(z) &= 1 + c_1 z + \dots + c_p z^p. \end{aligned}$$

(1) implies an input $\mathbf{u}(\cdot)$ at time $k-d$, produces an output $\mathbf{y}(k)$ at d time instants later. The next section describes how we formulate the class of minimum error variance controllers that predict the effect of actions $\mathbf{u}(\cdot)$ on states $\mathbf{y}(\cdot)$ such that a self-tuning adaptive controller is constructed.

A. Adaptive Neuro-Control Formulation

We use a universal function approximator to model the nonlinear plant dynamics in real-time and we design a model reference adaptive control (MRAC) system for the plant. Our contribution is that we use a recurrent NN (RNN) model in the form of the more powerful long short-term memory (LSTM) models, equipped with adequate number of neurons and hidden layers to model the plant dynamics. We also set up the control law in terms of the parameter estimates from the neural network output. The online parameter estimator ensures robustness in the presence of changing uncertainties. The adjustment mechanism is computed from Lyapunov analysis; this keeps the states of the system bounded under

closed-loop dynamics regardless of modeling uncertainties, parametric errors or states that are initialized outside the region of system stability. It also makes reference tracking robust in the presence of non-parametric uncertainties. For the multi-input, multi-output adjustable system

$$\dot{\mathbf{y}} = \mathbf{A}\mathbf{y} + \mathbf{B}\mathbf{\Lambda}(\mathbf{u} - f(\mathbf{y})) + \mathbf{w}(k) \quad (2)$$

with $\mathbf{y} \in R^n$, $\mathbf{u} \in R^m$; $\mathbf{A} \in R^{n \times n}$, $\mathbf{\Lambda} \in R^{m \times m}$ being unknown constant matrices, $\mathbf{B} \in R^{n \times m}$, $\text{sgn}(\mathbf{\Lambda})$ being known constant matrices, and $\mathbf{w}(k) \in R^n$ being a bounded time-varying unknown disturbance, upper-bounded by a fixed positive scalar \mathbf{w}_{max} . We make the following assumptions:

- a dynamic RNN with N neurons, $\varphi(\mathbf{y})$, exists that will map from a compact input space $\mathbb{U} \supset \mathbf{u}$ to an output space $\mathbf{y} \subset \mathbb{Y}$ on the Lebesgue integrable functions with closed interval $[0, T]$ or open-ended interval $[0, \infty)$;
- the nonlinear function $f(\mathbf{y})$ is exactly $\Theta^T \Phi(\mathbf{y})$ with coefficients $\Theta \in R^{N \times m}$ and a Lipschitz-continuous vector of basis functions $\Phi(\mathbf{y}) \in R^N$;
- inside a ball \mathbf{Y}_R of known, finite radius R , the ideal NN approximation $f(\mathbf{y}) : R^n \rightarrow R^m$, is realized to a sufficient degree of accuracy, $\varepsilon_f > 0$;
- the process noise $\mathbf{w}(k)$ is estimated alongside model parameters by the dynamic RNN and lumped into ε_f ;
- outside \mathbf{Y}_R , the NN approximation error can be upper-bounded by a known unbounded, scalar function $\varepsilon_{max}(\mathbf{y})$; $\|\varepsilon(\mathbf{y})\| \leq \varepsilon_{max}(\mathbf{y})$, $\forall \mathbf{y} \in \mathbf{Y}_R$;
- there exists an exponentially stable reference model

$$\dot{\mathbf{y}}_m = \mathbf{A}_m \mathbf{y}_m + \mathbf{B}_m \mathbf{r}, \quad (3)$$

with a Hurwitz matrix $\mathbf{A}_m \in R^{n \times n}$ and $\mathbf{B}_m \in R^{n \times m}$ commanded by a reference signal $\mathbf{r} \in R^m$. Our objective is to design an adaptive MRAC controller able to operate in the presence of parametric, ε_f , and non-parametric, $\mathbf{w}(k)$, uncertainties so as to assure the boundedness of all signals within the closed-loop dynamics. We postulate the following controller

$$\mathbf{u} = \hat{\mathbf{K}}_y^T \mathbf{y} + \hat{\mathbf{K}}_r^T \mathbf{r} + \hat{f}(\mathbf{y}). \quad (4)$$

where $\hat{\mathbf{K}}_y$ and $\hat{\mathbf{K}}_r$ are adaptive gains to be designed shortly. The $\hat{\mathbf{K}}_y^T \mathbf{y}$ term keeps the states of the approximation set $\mathbf{y} \in \mathbf{Y}_R$ stable, while the $\hat{\mathbf{K}}_r^T \mathbf{r}$ term causes the states to follow a given reference trajectory. The function approximator output $\hat{f}(\mathbf{y})$ ensures states that start outside the approximation set $\mathbf{y} \in \mathbf{Y}_R$ converge to \mathbf{Y}_R in finite time (it converges non-parametric errors ε_f that puts certain states out of the approximation set into \mathbf{Y}_R). We can generally write the approximator model as

$$\hat{f}(\mathbf{y}) = \hat{\Theta}^T \Phi(\mathbf{y}) + \varepsilon_f(\mathbf{y}),$$

where $\hat{\Theta}^T$ denotes the vectorized weights of the neural network and $\Phi(\mathbf{y})$ denotes the vector of lagged inputs and output defined as

$$\Phi(\mathbf{y}) = \{\mathbf{y}(k-d) \cdots \mathbf{y}(k-d-4), \mathbf{u}(k-d) \cdots \mathbf{u}(k-d-5)\}, \quad (5)$$

and $\varepsilon_f(\mathbf{y})$ is the approximation error. The closed-loop dynamics therefore become

$$\dot{\mathbf{y}} = \mathbf{A}\mathbf{y} + \mathbf{B}\mathbf{\Lambda} \left(\hat{\mathbf{K}}_y^T \mathbf{y} + \hat{\mathbf{K}}_r^T \mathbf{r} + \hat{f}(\mathbf{y}) - f(\mathbf{y}) \right). \quad (6)$$

We assume nonlinear function and approximator matching conditions, $f(\mathbf{y}) = \hat{f}(\mathbf{y})$, such that after rearrangement, (6) can be written as

$$\dot{\mathbf{y}} = (\mathbf{A} + \mathbf{B}\mathbf{\Lambda}\hat{\mathbf{K}}_y^T)\mathbf{y} + \mathbf{B}\mathbf{\Lambda}(\hat{\mathbf{K}}_r^T \mathbf{r} + \varepsilon_f(\mathbf{y})) \quad (7)$$

Furthermore, we assume model matching conditions with ideal constant gains \mathbf{K}_y and \mathbf{K}_r so that

$$\mathbf{A} + \mathbf{B}\mathbf{\Lambda}\mathbf{K}_y^T = \mathbf{A}_m, \quad \text{and} \quad \mathbf{B}\mathbf{\Lambda}\mathbf{K}_r^T = \mathbf{B}_m, \quad (8)$$

from which

$$\begin{aligned} \mathbf{A} + \mathbf{B}\mathbf{\Lambda}\hat{\mathbf{K}}_y^T - \mathbf{A}_m &= \mathbf{B}\mathbf{\Lambda}\tilde{\mathbf{K}}_y^T \text{ and} \\ \mathbf{B}\mathbf{\Lambda}\hat{\mathbf{K}}_r^T - \mathbf{B}_m &= \mathbf{B}\mathbf{\Lambda}\tilde{\mathbf{K}}_r^T, \end{aligned} \quad (9)$$

where $\tilde{\mathbf{K}}_y^T = \mathbf{K}_y^T - \hat{\mathbf{K}}_y^T$ and $\tilde{\mathbf{K}}_r^T = \mathbf{K}_r^T - \hat{\mathbf{K}}_r^T$. The generalized error state vector $\mathbf{e}(k) = \mathbf{y}(k) - \mathbf{y}_m(k)$, has dynamics $\dot{\mathbf{e}}(k) = \dot{\mathbf{y}}(k) - \dot{\mathbf{y}}_m(k)$, such that by substituting (3) and (6) into $\dot{\mathbf{e}}$, we have

$$\dot{\mathbf{e}}(k) = \mathbf{A}_m \mathbf{e}(k) + \mathbf{B}\mathbf{\Lambda}[\tilde{\mathbf{K}}_r^T \mathbf{r} + \tilde{\mathbf{K}}_y^T \mathbf{y} - \varepsilon_f(\mathbf{y}(k))] \quad (10)$$

The estimation error will be bounded as long as $\mathbf{y} \in \mathbf{Y}_R$. Our goal is to keep $\mathbf{y} \in \mathbf{Y}_R$.

Proposition: Given correct choice of adaptive gains $\hat{\mathbf{K}}_y$ and $\hat{\mathbf{K}}_r$, the error vector, $\mathbf{e}(k)$ with closed loop time derivative given by (10) is uniformly ultimately bounded, and the state \mathbf{y} will converge to a neighborhood of \mathbf{r} .

Proof: We construct a stability analysis of a suitable MRAC system by choosing a Lyapunov function candidate V in terms of the generalized error state space \mathbf{e} , gains, $\tilde{\mathbf{K}}_y^T$, $\tilde{\mathbf{K}}_r^T$, and parameter error $\varepsilon_f(\mathbf{y}(k))$ space ([17], [18], [19]) as follows

$$\begin{aligned} V(\mathbf{e}, \tilde{\mathbf{K}}_y, \tilde{\mathbf{K}}_r) &= \mathbf{e}^T \mathbf{P} \mathbf{e} + \text{tr}(\tilde{\mathbf{K}}_y^T \Gamma_y^{-1} \tilde{\mathbf{K}}_y | \Lambda) \\ &\quad + \text{tr}(\tilde{\mathbf{K}}_r^T \Gamma_r^{-1} \tilde{\mathbf{K}}_r | \Lambda) \end{aligned} \quad (11)$$

where Γ_y and Γ_r are fixed symmetric, positive definite (SPD) matrices of adaptation rates. Let $\text{tr}(\mathbf{A})$ denote the trace of matrix \mathbf{A} . \mathbf{P} is a unique SPD matrix solution of the algebraic Lyapunov function

$$\mathbf{P}\mathbf{A}_m + \mathbf{A}_m^T \mathbf{P} = -\mathbf{Q}, \quad (12)$$

where \mathbf{Q} is a SPD matrix. Take the time derivative of (11)

$$\begin{aligned} \dot{V}(\mathbf{e}, \tilde{\mathbf{K}}_y, \tilde{\mathbf{K}}_r, \varepsilon_f) &= \dot{\mathbf{e}}^T \mathbf{P} \mathbf{e} + \mathbf{e}^T \dot{\mathbf{P}} \mathbf{e} + 2\text{tr}(\tilde{\mathbf{K}}_y^T \Gamma_y^{-1} \dot{\tilde{\mathbf{K}}}_y | \Lambda) \\ &\quad + 2\text{tr}(\tilde{\mathbf{K}}_r^T \Gamma_r^{-1} \dot{\tilde{\mathbf{K}}}_r | \Lambda) \\ &= \mathbf{e}^T (\mathbf{P}\mathbf{A}_m + \mathbf{A}_m^T \mathbf{P}) \mathbf{e} + 2\mathbf{e}^T \mathbf{P} \mathbf{B} \mathbf{\Lambda} \left(\tilde{\mathbf{K}}_y^T \mathbf{y} + \tilde{\mathbf{K}}_r^T \mathbf{r} - \varepsilon_f(\mathbf{y}) \right) \\ &\quad + 2\text{tr} \left(\tilde{\mathbf{K}}_y^T \Gamma_y^{-1} \dot{\tilde{\mathbf{K}}}_y | \Lambda \right) + 2\text{tr} \left(\tilde{\mathbf{K}}_r^T \Gamma_r^{-1} \dot{\tilde{\mathbf{K}}}_r | \Lambda \right) \end{aligned}$$

$$= -\mathbf{e}^T \mathbf{Q} \mathbf{e} - 2\mathbf{e}^T \mathbf{P} \mathbf{B} \Lambda \varepsilon_f(\mathbf{y}) + 2\mathbf{e}^T \mathbf{P} \mathbf{B} \Lambda \tilde{\mathbf{K}}_y^T \mathbf{y} \\ + 2 \operatorname{tr} \left(\tilde{\mathbf{K}}_y^T \Gamma_y^{-1} \dot{\hat{\mathbf{K}}}_y \right) + 2\mathbf{e}^T \mathbf{P} \mathbf{B} \Lambda \tilde{\mathbf{K}}_r^T \mathbf{r} + 2 \operatorname{tr} \left(\Delta \mathbf{K}_r^T \Gamma_r^{-1} \dot{\hat{\mathbf{K}}}_r \right)$$

Recall $x^T y = \operatorname{tr}(y x^T)$ from trace identity, so that

$$\dot{V}(\cdot) = -\mathbf{e}^T \mathbf{Q} \mathbf{e} - 2\mathbf{e}^T \mathbf{P} \mathbf{B} \Lambda \varepsilon_f(\mathbf{y}) \\ + 2 \operatorname{tr} \left(\tilde{\mathbf{K}}_y^T (\Gamma_y^{-1} \dot{\hat{\mathbf{K}}}_y + \mathbf{y}^T \mathbf{P} \mathbf{B} \operatorname{sgn}(\Lambda)) \right) |\Lambda| \quad (13) \\ + 2 \operatorname{tr} \left(\tilde{\mathbf{K}}_r^T (\Gamma_r^{-1} \dot{\hat{\mathbf{K}}}_r + \mathbf{r}^T \mathbf{P} \mathbf{B} \operatorname{sgn}(\Lambda)) \right) |\Lambda|$$

where for a real-valued x , $x = \operatorname{sgn}(x)|x|$. The first two terms in (13) will be negative definite for all $\mathbf{e} \neq 0$ since \mathbf{A}_m is Hurwitz and the other terms in (13) will be identically null if we choose the adaptation laws

$$\dot{\hat{\mathbf{K}}}_y = -\Gamma_y \mathbf{y} \mathbf{e}^T \mathbf{P} \mathbf{B} \operatorname{sgn}(\Lambda), \quad \dot{\hat{\mathbf{K}}}_r = -\Gamma_r \mathbf{r} \mathbf{e}^T \mathbf{P} \mathbf{B} \operatorname{sgn}(\Lambda). \quad (14)$$

The time-derivative of the Lyapunov function can then be written as

$$\dot{V}(\cdot) = -\mathbf{e}^T \mathbf{Q} \mathbf{e} - 2\mathbf{e}^T \mathbf{P} \mathbf{B} \Lambda \varepsilon_f(\mathbf{y}) \\ \leq -\lambda_{low} \|\mathbf{e}\|^2 + 2\|\mathbf{e}\| \|\mathbf{P} \mathbf{B}\| \lambda_{high}(\Lambda) \varepsilon_{max}(\mathbf{y}), \quad (15)$$

where $\lambda_{low}, \lambda_{high}$ represent the minimum and maximum characteristic roots of \mathbf{Q} and Λ respectively. $\dot{V}(\cdot)$ is thus negative definite outside the compact set

$$\chi = \left(\mathbf{e} : \|\mathbf{e}\| \leq \frac{2\|\mathbf{P} \mathbf{B}\| \lambda_{high}(\Lambda) \varepsilon_{max}(\mathbf{y})}{\lambda_{low}(\mathbf{Q})} \right). \quad (16)$$

and we conclude that the error \mathbf{e} is *uniformly ultimately bounded*. As \mathbf{e} converges to a neighborhood of 0, \mathbf{y} converges to a neighborhood of \mathbf{y}_m . From the stable model reference system in (3), \mathbf{y} converges to a neighborhood of \mathbf{r} .

VI. EXPERIMENT: SOFT-ROBOTS CONTROL

The headpose is determined based on our formulation in IV. The pose of the head is made up of the tuples $\{x(k), y(k), z(k), \theta(k), \psi(k)\}$. Since we are only controlling the states $\{z(k), \theta(k), \psi(k)\}$, we discard the x , and y terms.

A. Network Design

The nonlinear function $f(\mathbf{y})$ in (2) is modeled with a real-time long short-term memory (LSTM [20])-RNN variant due to its capacity for long-term context memorization and inherent multiplicative units that avoid oscillating weights or vanishing gradients when error signals are backpropagated in time [20], [21]. LSTMs truncate gradients in the network where it is harmless by enforcing constant error flows through their *constant error carousels*. As a result, LSTMs are robustly more powerful for adaptive sequence-to-sequence modeling or mapping data that temporally evolve in time. Their biological model makes them more suitable for adaptive robotics such as soft robots than previously used artificial NNs such as feedforward networks [22], radial basis-functions [19], [23] or vanilla RNNs [24].

We require accurate mapping of temporally lagged patterns in inputs to output states, a dynamic model of nonlinear solenoid valve encoder values to sensor measurements, and a dynamic model that stores high-precision network gradients

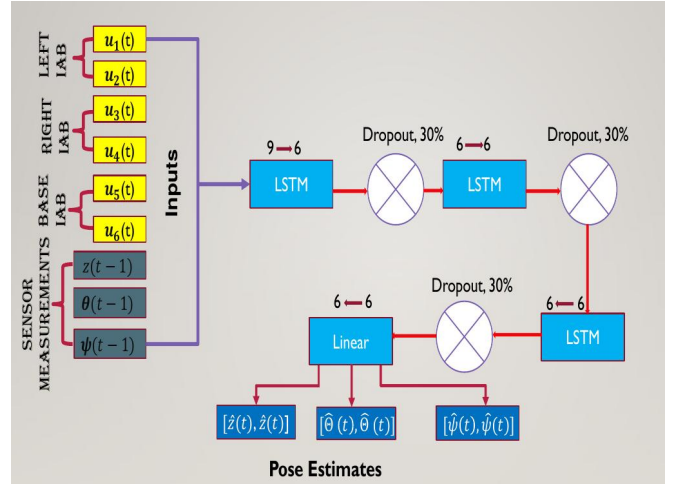


Fig. 3: Function Approximator Architecture

with low computational costs. These are characteristic traits of LSTM networks given their capacity for nonlinearity approximation and their $O(1)$ single-pass computational time, so we chose the LSTM model of Hochreiter [20] in modeling $f(\mathbf{y})$. The real-time NN model takes a memory-based 1-D vector of current inputs and past outputs as in (5), propagates them through three hidden layers, with each layer made up of $\{9, 6, 6\}$ neurons respectively, and we apply 30% dropout (Hinton et al. [25]) after each hidden layer to avoid overfitting. The last layer is a fully connected linear layer that maps the nonlinear transformations of the previous hidden layers into a 6-vector output. The architecture of the neuro-controller is shown in Fig. 3. The last layer is designed to temporally generate appropriate control actions, which together with the regulation component and feedback component of (4) ensures robustness of the control scheme to non-parametric uncertainties. This visuo-controller maps states to the torques that control the solenoid valves. The overall network has neuron connection weights and thresholds of approximately 1,400. This makes search for a suitable visuo-controller feasible. Our contribution is that we train an online neural network whose weights converge to a global optimum over time in order to keep the head in bounded command-reference tracking mode.

The LSTM model estimates a mathematical model $f(\mathbf{y})$, that minimizes the mean-squared errors between predicted output $\hat{\mathbf{y}}(k)$ and actual output $\mathbf{y}(k)$ according to

$$f(\mathbf{y}(k)) = \arg \min_w V_N(w, \Phi(\mathbf{y})) \quad (17)$$

where $V_N(w, \Phi(\mathbf{y})) = \sum_{t=1}^K \sum_{i=1}^n \frac{1}{2} (\hat{\mathbf{y}}_i(t) - \mathbf{y}_i(t))^2$, $\Phi(\mathbf{y})$ is as defined in (5) on a bounded interval $[1, N]$. (17) is minimized using stochastic gradient descent so that at each iteration, we update the parameters (weights) of the network \mathbf{w}_i based on the *ordered derivatives* of $V_N(\mathbf{w}, \Phi(\mathbf{y}))$ (Werbos

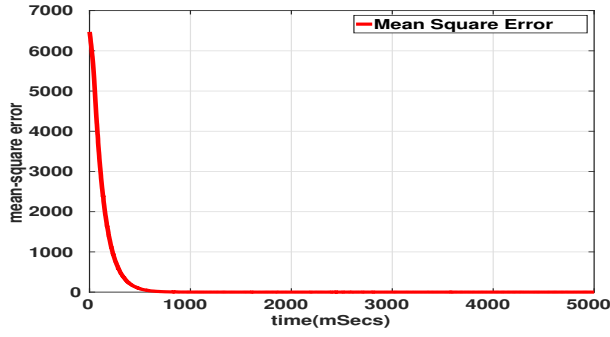


Fig. 4: Mean Square Error of Neural Network Controller During Training.

[26]) *i.e.*

$$\mathbf{w}_{k+1} \leftarrow \eta \mathbf{w}_k - \alpha \sum_{i=1}^n \nabla_{\mathbf{w}} V(\mathbf{y}_i, \hat{\mathbf{y}}_i(\theta_k)). \quad (18)$$

η hastens the optimization in a direction of low but steepest descent in training error, and α is a sufficiently small learning rate, and $\nabla_{\mathbf{w}} V(\theta, \Phi(\mathbf{y}))$ is the derivative of V with respect to \mathbf{w} averaged over the k -th batch (we used a single batch size).

B. Network Training and Control Parameters

We fixed the systems' random number seed at the start of every experiment to assure repeatable performance; this was set to 123. α in (18) is set to 0.005 and we initialized the weights of Fig. 3 from a one-dimensional normal distribution tensor with zero-mean and unit variance. The result from the function approximator error is shown in Fig. 4. It takes 5 seconds for the network to reach a global minimum which is sufficient in a typical clinical setup. \mathbf{y}_m in (3) is computed based on the solution to the forced response of the linear system,

$$\mathbf{y}_m(t) = e^{\mathbf{A}_m t} \mathbf{y}_m(0) + \int_0^t e^{\mathbf{A}_m(t-\tau)} \mathbf{B}_m \mathbf{r}(\tau) d\tau.$$

For a settling time requirement $T_s = 5 \text{secs}$ at which the response remains within 2% of final value, we find

$$\mathbf{A}_m = \begin{bmatrix} -\frac{1334}{1705} & 0 & 0 \\ 0 & -\frac{1334}{1705} & 0 \\ 0 & 0 & -\frac{1334}{1705} \end{bmatrix}. \quad (19)$$

LaSalle's theorem implies that for a nonnegative \mathbf{Q} and a given positive definite \mathbf{P} , the pair $(\mathbf{Q}, \mathbf{A}_m)$ will be observable so that the dynamical system is globally asymptotically stable. After searching, we picked a positive definite \mathbf{Q} for the dissipation energy in (15) as $\mathbf{Q} = \text{diag}(100, 100, 100)$ and set $\mathbf{\Lambda} = I_{3 \times 3}$ so that solving the general form of the lyapunov equation, we have

$$\mathbf{P} = \begin{bmatrix} -\frac{170500}{2668} & 0 & 0 \\ 0 & -\frac{170500}{2668} & 0 \\ 0 & 0 & -\frac{170500}{2668} \end{bmatrix} \quad (20)$$

The six solenoid valves are operating in pairs so that two solenoid valves create a difference in air mass within each IAB at any given time. We therefore choose a \mathbf{B} matrix that maps control signals based on encoder values of the valves. We found

$$\mathbf{B} = \begin{bmatrix} 1 & 400 & 0 & 0 & 0 & 0 \\ 0 & 0 & 1 & 400 & 0 & 0 \\ 0 & 0 & 0 & 0 & 1 & 1 \end{bmatrix} \quad (21)$$

to be suitable. The 1 terms in (21) denote the maximum duty-cycle that can be applied to the Dakota valves based on the software configuration of the NI RIO PWM generator; 400 is the corresponding maximum encoder value of the variable current source signals generated from the RIO device to control the PVQ valves. The last linear layer of the network that corresponded to the Dakota valves was transformed to the range $[0, 1]$ using the sigmoid function while the outputs that generated the *PVQ* torques was transformed with the function

$$g_{pvq}(x) = \frac{400}{1 + \exp(-x)} \quad (22)$$

since at a value of 200 the valve starts opening and reaches maximum open value at 400. $\hat{\mathbf{K}}_y$ and $\hat{\mathbf{K}}_r$ in (14), were obtained by solving the ODEs iteratively using a single step of the integral of the solutions to $\hat{\mathbf{K}}_y(t)$, $\hat{\mathbf{K}}_r(t)$; our step-size was chosen as 0.01. Our solution is an implementation of the Runge-Kutta Dormand-Prince 5 ODE-solver available in the Boost C++ Libraries².

C. Results and Discussion

Since the height, pitch and roll of the head are coupled through the ball joints, arbitrary head pose cannot be achieved. The head was moved to multiple points, and the pose was extracted, giving a set of achievable goal positions. Control experiments were then performed to move the head back to the goal positions.

Fig. 5 show the performance of the controller moving the head from $[z, \theta, \psi]^T = [2.5 \text{mm}, 25^\circ, 35^\circ]^T$ to goal pose $[14 \text{mm}, 1.6^\circ, 45^\circ]^T$, *i.e.* the head is move up and faced to its left. The controller successfully enforces compliance of the head to the defined 3-DOF axes reference trajectory motion correction system within 20 seconds.

VII. CONCLUSIONS

Accurate patient position correction during frameless and maskless radiotherapy is critical to a successful clinical operation. In this work, we presented a soft-robot system for motion compensation, along with a robust adaptive neurocontroller to intelligently correct a patient's deviation from planned positions. The result is promising showing that given a reference command along a Cartesian and two orientation axes, an adequate error correction mechanism is achievable in real-time to a sub-degree and millimeter level of accuracy for real-time control. Unlike related works that employ radiation attenuating devices such as stepper

²<https://goo.gl/17JyYe>

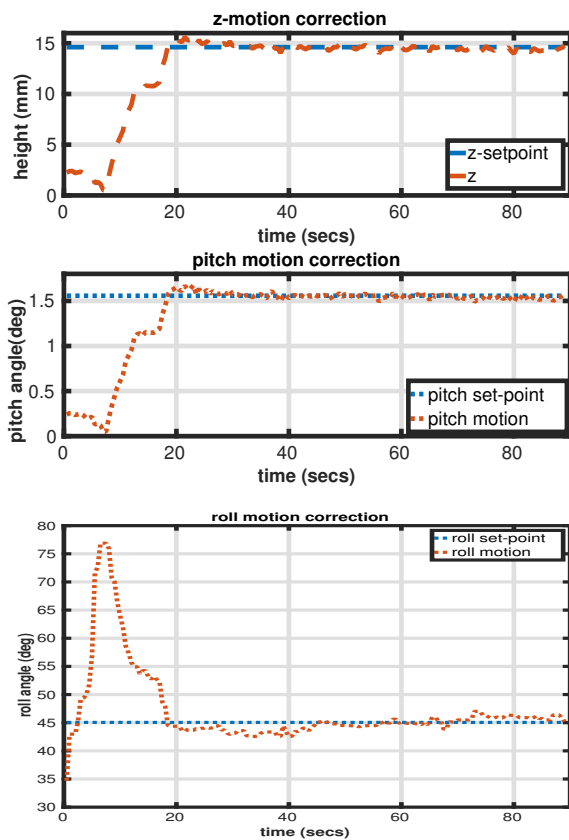


Fig. 5: Results of correcting the motions of the head along the camera's principal axis, and orienting the head along the pitch and roll axes respectively.

motors positioned underneath the patient's head on the table, our proposal eliminates the reduction in the efficiency of dosage plans by using soft elastomeric polymers in correcting patient's deviation from treatment plans.

In subsequent work, we will focus on decoupling the control laws for the coupled states of the system so that the controlling pitch or z-motion or x- and yaw-motion can be independently achieved whilst reaching desired overall goal. We will also extend these preliminary 3-DOF control algorithm to a 6-DOF IAB soft-robot system on a mannequin with head and torso and volunteer human trials.

REFERENCES

- [1] O. A. Zeidan, K. M. Langen, S. L. Meeks, R. R. Manon, T. H. Wagner, T. R. Willoughby, D. W. Jenkins, and P. A. Kupelian, "Evaluation of image-guidance protocols in the treatment of head and neck cancers," *International Journal of Radiation Oncology* Biology* Physics*, vol. 67, no. 3, pp. 670–677, 2007.
- [2] F. Sterzing, R. Engenhardt-Cabillic, M. Flentje, and J. Debus, "Image-guided radiotherapy," *Deutsches Aerzteblatt International*, vol. 108, no. 16, 2011.
- [3] O. Ogunmolu, X. Gu, S. Jiang, and N. Gans, "A real-time soft robotic patient positioning system for maskless head-and-neck cancer radiotherapy: An initial investigation," in *IEEE International Conference on Automation Science and Engineering*, Gothenburg, Sweden, Aug 2015.
- [4] —, "Visual-servoing Control of a Soft Robot," in *IEEE International Conference on Automation Science and Engineering*, Fort Worth, Texas, Aug 2016.

- [5] J. Rossiter and H. Hauser, "Soft robotics - the next industrial revolution? [industrial activities]," *IEEE Robotics Automation Magazine*, vol. 23, no. 3, pp. 17–20, Sept 2016.
- [6] S. Sastry and M. Bodson, *Adaptive Control: Stability, Convergence, and Robustness*. Prentice-Hall Advanced Reference Series, Englewood Cliffs, New Jersey, 1989.
- [7] L. I. Cerviño, N. Detorie, M. Taylor, J. D. Lawson, T. Harry, K. T. Murphy, A. J. Mundt, S. B. Jiang, and T. A. Pawlicki, "Initial clinical experience with a frameless and maskless stereotactic radiosurgery treatment," *Practical radiation oncology*, vol. 2, no. 1, pp. 54–62, 2012.
- [8] L. I. Cerviño, T. Pawlicki, J. D. Lawson, and S. B. Jiang, "Frame-less and Mask-less Cranial Stereotactic Radiosurgery: A Feasibility Study," *Phys. Med. Biol.*, vol. 55, pp. 1863–1873, 2010.
- [9] G. Li, A. Ballangrud, M. Chan, R. Ma, K. Beal, Y. Yamada, T. Chan, J. Lee, P. Parhar, J. Mechalakos, *et al.*, "Clinical experience with two frameless stereotactic radiosurgery (fsrs) systems using optical surface imaging for motion monitoring," *Journal of applied clinical medical physics/American College of Medical Physics*, vol. 16, no. 4, p. 5416, 2015.
- [10] X. Liu, A. H. Belcher, Z. Grelewicz, and R. D. Wiersma, "Robotic stage for head motion correction in stereotactic radiosurgery," in *American Control Conference (ACC), 2015*. IEEE, 2015, pp. 5776–5781.
- [11] E. GmBh. Flexview. Accessed on January 21, 2016. [Online]. Available: <http://www.ensenso.com/products/flexview/>
- [12] R. B. Rusu, "Semantic 3d object maps for everyday manipulation in human living environments," *PhD thesis*, 2009.
- [13] P. H. Torr and A. Zisserman, "Mlesac: A new robust estimator with application to estimating image geometry," *Computer Vision and Image Understanding*, vol. 78, no. 1, pp. 138–156, 2000.
- [14] R. B. Rusu, Z. C. Marton, N. Blodow, M. E. Dolha, and M. Beetz, "Functional object mapping of kitchen environments," *2008 IEEE/RSJ International Conference on Intelligent Robots and Systems, IROS*, pp. 3525–3532, 2008.
- [15] R. B. Rusu and S. Cousins, "3D is here: Point Cloud Library (PCL)," in *IEEE International Conference on Robotics and Automation (ICRA)*, Shanghai, China, May 9-13 2011.
- [16] R. B. Rusu, A. Holzbach, M. Beetz, and G. Bradski, "Detecting and segmenting objects for mobile manipulation," in *Computer Vision Workshops (ICCV Workshops), 2009 IEEE 12th International Conference on*. IEEE, 2009, pp. 47–54.
- [17] P. Parks, "Liapunov Redesign of Model Reference Adaptive Control Systems," *IEEE Transactions on Automatic Control*, vol. 11, no. 3, pp. 362–367, 1966.
- [18] Y. D. Landau, *Adaptive Control: The Model Reference Approach*. Marcel Dekker, Inc, 1979.
- [19] E. Lavretsky and K. Wise, *Robust Adaptive Control with Aerospace Applications*. Springer, 2005.
- [20] S. Hochreiter and J. Schmidhuber, "Long short-term memory," *Neural computation*, vol. 9, no. 8, pp. 1735–80, 1997.
- [21] B. Y. et al., "Learning long-term dependencies with gradient descent is difficult," *IEEE Transactions on Neural Networks*, 1994, doi: 10.1109/72.279181.
- [22] H. Dinh, S. Bhasin, R. Kamalapurkar, and W. E. Dixon, "Dynamic Neural Network-based Output Feedback Tracking Control for Uncertain Nonlinear Systems," *Journal of Dynamic Systems, Measurement, and Control*, 2017.
- [23] H. Patino and D. Liu, "Neural network-based model reference adaptive control system," *IEEE Transactions on Systems, Man, and Cybernetics, Part B (Cybernetics)*, vol. 30, no. 1, pp. 198–204, 2000.
- [24] J. S. Wang and Y. P. Chen, "A Fully Automated Recurrent Neural Network for Unknown Dynamic System Identification and Control," *IEEE Transactions on Circuits and Systems*, vol. 53, 2006.
- [25] N. Srivastava, G. Hinton, A. Krizhevsky, I. Sutskever, and R. Salakhutdinov, "Dropout : A Simple Way to Prevent Neural Networks from Overfitting," *Journal of Machine Learning Research (JMLR)*, 2014.
- [26] P. J. Werbos, "Backpropagation Through Time: What It Does and How to Do It," *Proceedings of the IEEE*, vol. 78, no. 10, pp. 1550–1560, 1990.